Technical Notes
July 2025
Issue TN0301

ESYDA - Earth System modelling and data assimilation division

A multi-scale unstructured mesh model for simulating sea ice

By **Francesco Cocetta, Doroteaciro Iovino, Lorenzo Zampieri***
CMCC Foundation - Euro-Mediterranean Center on Climate Change, Italy

* *now at European Centre for Medium-Range Weather Forecasts*

Corresponding author address: francesco.cocetta@cmcc.it

This work was supported by the European Union's NextGenerationEU and the Horizon Europe project EDITO-Model Lab (grant No 101093293).

SUMMARY

Under rapidly changing climate conditions, sea ice is undergoing profound physical and thermodynamic transformations. These include changes in thickness, spatial extent, melt dynamics, and surface characteristics such as melt ponds and open water fractions. In addition, its temporal variability of sea ice is changing significantly, with shifts in the onset and duration of the freezing and melting seasons, as well as increased interannual and seasonal fluctuations. Accurately capturing these evolving regimes requires sea ice models capable of simulating not only traditional conditions but also the emerging behaviours and feedbacks associated with a warmer, more variable polar environment. This calls for greater model flexibility, finer spatial and temporal resolution, and advanced parameterisations that reflect the emerging sea ice regimes. In response to this need, the Foundation Euro-Mediterranean Center on Climate Change (CMCC) is actively developing a high-complexity sea ice module within the global coastal ocean model MUSE (multiscale unstructured model for Simulating the Earth water environment). MUSE is a general ocean circulation model based on finite-element discretisation on unstructured meshes; it is designed to enable simulations of both global and coastal ocean-sea ice interactions for research and operational purposes. The sea ice module, MUSE-I, integrates an elastic-viscous-plastic dynamic solver with thermodynamic column physics and advection scheme to represent the sea ice state and its evolution on spatially adaptive meshes. This report presents a comprehensive overview of MUSE-I, detailing its integration within the MUSE framework and showcasing its capabilities through a series of representative case studies.

CONTENT

1. INTRODUCTION

Over the past several decades, global ocean models have served as essential investigation tools for a wide range of scientific and applied fields. These include climate change projections, weather and seasonal forecasting, and studies of ocean circulation and thermohaline processes, but also coastal dynamics and sea level rise studies, and interaction with biological processes. Additionally, ocean models are applied to oil spill and pollutant dispersion studies, as well as in operational oceanography for real-time monitoring, navigation, and emergency response.

Within the global domain, polar regions have been a primary focus of ocean modelling efforts for a variety of reasons. In these areas, sea ice is a fundamental component of the climate system. Ocean models play a crucial role in representing the presence and dynamics of sea ice by simulating its formation, drift, deformation, and melting, as well as its complex interactions with both oceanic and atmospheric processes. Accurate representation of these processes is essential for understanding the unique feedback mechanisms that characterise high-latitude environments.

Although sea ice accounts for only a small fraction of the Earth's total ice volume, when in its February minimum, it covers an average extent of approximately $18 \times 10^6 km^2$ (1979-2020) across both the Northern and Southern hemispheres combined [31], equivalent to approximately 5% of the global ocean surface. Given its extensive coverage, which varies across time and space, the processes governing the formation, evolution, and melting of sea ice must be accurately understood and represented, together with ocean dynamics, to provide reliable information to scientists, policymakers, and other stakeholders. Given its extensive coverage, sea ice plays a role of prime importance in the climate system and for human activities, and therefore, processes leading to the formation, evolution, and melting of this medium need to be simulated with appropriate models in conjunction with the ocean to provide accurate information to stakeholders.

In recent years, the CMCC Foundation has initiated the implementation of a new global ocean model to support applications in the global coastal ocean domain, which require high spatial and temporal resolution in selected regions, alongside flexibility and computational efficiency. To meet these demands, the model employs an unstructured mesh for domain discretisation, allowing it to bridge scale gaps between global climate processes, basin-scale circulation, and regional or local dynamics through multi-resolution capability and geometric adaptability. The ability of unstructured-mesh ocean models to capture multiscale interactions makes them a powerful alternative to traditional structured-grid models in both scientific and operational contexts, as demonstrated by state-of-the-art systems such as FESOM2 [39, 38], MPAS-Ocean [32], and ICON [25]. The new CMCC ocean model, named MUSE (Multiscale Unstructured Model for Simulating the Earth's Water Environment), is designed for research and applications in the global coastal ocean. Given the global scope of MUSE, incorporating a numerical representation of the sea ice system is essential for obtaining realistic simulations in polar regions. The objective of this report is to present the main features of the MUSE sea ice module (hereafter referred to as MUSE-I), describe its implementation within the model framework, and provide a preliminary assessment of its performance.

The manuscript is organised as follows. Section 2 outlines the main physical characteristics of MUSE-I, including its coupling with the ocean component and a summary of key technical aspects related to model implementation (e.g. initialisation, output management, and restart capabilities). Section 3 briefly presents the experimental configuration and model setup employed in the test simulations analysed in the report (e.g., simulation protocol, computational mesh, external forcing fields), and then delves into the analysis of a set of global multi-year simulations performed with the coupled ocean-sea ice system to showcase the potential of the sea ice module and evaluate its performance in both polar regions. Section 4 summarises the work and main outcomes, and also outlines future development plans for MUSE-I.

2. MODEL DESCRIPTION

The MUSE-I model is the high-complexity sea ice module developed for MUSE, the global coastal ocean system based on the three-dimensional hydrodynamic model described in [30]. The dynamical core of MUSE employs the finite element method to solve the three-dimensional hydrodynamic equations formulated as primitive equations. In the horizontal dimension, the code employs unstructured triangular surface meshes and the vertical discretisation is based on the geopotential z* coordinate system. This section provides a scientific and technical description of MUSE-I, as a part of MUSE. The sea ice module does not exist as a stand-alone version, so it relies on infrastructure and mesh partitioning of the ocean component.

This model component adopts widely recognised methodologies that are standard in sea ice modelling. Firstly, MUSE-I adopts the continuum assumption, a fundamental simplification that treats the sea ice cover as a continuous and deformable medium, rather than as a collection of discrete ice floes. The model equations describe the average behaviour of sea ice floes within the grid-cell scale, neglecting the detailed interactions between individual floes that occur at sub-grid scales. This approach allows for the application of continuum mechanics to describe the large-scale behaviour of the ice, enabling the use of partial differential equations to represent processes such as deformation, drift, and thermodynamic evolution. It has proven adequate across a wide range of spatial resolutions, from several hundred kilometres down to the kilometre scale, encompassing the target resolution of MUSE and its intended applications. Physical processes acting on sea ice can be divided into two categories: halo-thermodynamic processes, which involve the transfer of heat or radiation, and dynamic processes, which move and deform the ice. MUSE-I adopts the so-called 2+1 split assumption, whereby the one-dimensional vertical dimension is treated independently from the two-dimensional horizontal domain. Specifically, halo-thermodynamic processes are solved exclusively in the vertical direction, while sea ice dynamics are resolved in the horizontal plane. A direct consequence of this assumption is that the model does not account for vertical displacements of sea ice or horizontal heat transfer between adjacent grid cells. However, these processes are generally negligible in the context of large-scale geophysical applications.

MUSE-I adopts a modular design, which facilitates the development of individual components of the code and enables adaptable model complexity, tailored to the needs of different scientific investigations and applications. The model comprises multiple interrelated components: an independent sub-module that simulates all vertical processes, and a sea ice dynamics model that includes an advection scheme for the prognostic model tracers. These components are described in the following sections, along with an overview of the coupling between the sea ice and ocean components and the model's input/output (I/O) capabilities.

2.1 THERMODYNAMIC PROCESSES

Ice thermodynamics refers to the processes involving energy transfer within and through sea ice, which govern how ice forms, grows, melts, and stores energy. These processes include heat conduction, radiative exchange, latent heat transfer, and sensible heat flux, and collectively determine the net growth or melting of the ice.

The thermodynamic processes in MUSE-I are handled by a dedicated module based on the Icepack framework (v1.4.0; [19]). This module is implemented as a stand-alone component, which can be configured and run independently of the rest of the model. It is a collection of physical parametrisations that account for halo-thermodynamic and mechanical sub-grid processes not explicitly resolved by the hosting sea-ice code. Its modular implementation allows for varying substantially the complexity of the sea-ice model, with the possibility of choosing between several schemes and a broad set of active and passive tracers that describe the sea-ice state. The main physical processes simulated by this module are the sea ice thermodynamics, the sea ice interaction with solar radiation, and the mechanical redistribution of sea ice, which describes the sea ice thickening due to ridging and rafting when this medium undergoes shear and/or compressive stresses. Furthermore, it allows for a comprehensive description of sea ice biogeochemistry (BGC) and isotope transport.

In reality, sea ice regions often consist of a complex mixture of open water, thin first-year ice, thicker multiyear ice, and thick ridges formed by the breaking and convergence of ice floes. To represent this variability, the module is configured with four distinct tiles, each corresponding to a specific sea ice condition: open water, slab ice with uniform thickness and no snow cover, a full ice thickness distribution (ITD), and land. All tiles are subjected to the same atmospheric forcing, and no interactions or exchanges occur between them.

The model parameterisations are designed to evolve, over time, a set of prognostic tracers that describe their snow/ice properties. Among the tracers implemented in MUSE-I, the most relevant include the sea ice area fraction, sea ice volume per unit area, enthalpy of sea ice and snow, internal sea ice salinity, melt pond fraction and volume, and the ridged-ice area fraction. Within each grid cell, these tracers are defined across multiple thickness categories, allowing the model to capture the evolution of **ice thickness distribution** (ITD) in time and space. This approach has become the standard in many sea ice models, including SI3 [43], CICE [22], and FESIM2 [7]. The use of ITD is particularly beneficial for representing non-linear, thickness-dependent processes such as horizontal transport, ridging, and other mechanical deformations, as well as thermodynamic growth and melt across different ice thicknesses. Since heat conduction is proportional to the vertical temperature gradient, thin ice tends to grow and melt more rapidly than thicker ice and is more susceptible to mechanical deformation. As sea ice undergoes thermodynamic growth and melting, the ITD within a model grid cell evolves through transport in thickness space. To capture this evolution, an incremental remapping method is employed, similar to that described by [23], while the mechanical redistribution is parametrised following the approaches of [41], [37], [13], and [28]. These parameterisations are applied after the horizontal transport step and are designed to convert thinner ice into thicker ice during episodes of sea ice convergence while ensuring that the total ice area remains within the bounds of the model grid cell. The ITD, denoted as $g(h, \mathbf{x}, t)$, describes the probability $g(h)\,dh$ of finding sea ice within the thickness range $(h, h + dh)$ at a given time and location. The distribution integrates all physical processes that influence sea ice volume:

$$\frac{\partial g}{\partial t} = -\nabla \cdot (g\mathbf{u}) + \Psi - \frac{\partial}{\partial h}(fg) + \mathcal{L} \tag{1}$$

where $\mathbf{u}$ is the horizontal sea ice velocity, $\nabla = \left(\frac{\partial}{\partial x}, \frac{\partial}{\partial y}\right)$ is the horizontal gradient operator, f is the rate of thermodynamic ice growth or melt, Ψ is the mechanical redistribution function (e.g., ridging, rafting), and $\mathcal{L}$ represents lateral melting. The four terms on the right-hand side describe the horizontal transport of ice in physical space, mechanical redistribution (e.g., due to ridging and rafting), vertical transport in thickness space due to thermodynamic growth or melt, and lateral melting, which replaces ice with open water. User-customised parameters set the number of ITD categories and the ITD discretisation function among the coded options. For each ITD class, the sea ice and snow are further discretised in multiple vertical layers (their number can also be customised by the user), useful for representing vertical tracers' variation within sea ice (enthalpy, salinity).

It is worth mentioning that, in parallel to the ITD, the module implements a **Floe Size Distribution** (FSD; [35]), which is relevant for refining the simulation of sea ice processes such as lateral melting and sea ice-waves interaction [34]. While we implemented all the FSD-relevant subroutines in MUSE-I, we have yet to test them extensively due to the absence of a wave component in MUSE. The reader should note that while the number of ITD classes, FSD classes, and vertical layers can be varied arbitrarily according to users' needs, finer subgrid discretisation requires higher computational, memory, and storage capacity.

For each thickness category, the model computes changes in the ice and snow thickness and vertical temperature profile resulting from radiative, turbulent, and conductive heat fluxes [5]. The ice has a temperature-dependent specific heat to simulate the effect of brine pocket melting and freezing when ice salinity is accounted for.

Thermodynamic components of sea ice models treat the ice as a multi-layer slab with energy fluxes at both surfaces. The **net surface energy flux** from the atmosphere to the ice (with all fluxes defined as positive downward) is

$$q\frac{dh}{dt} = F_s + F_l + F_{L\downarrow} + F_{L\uparrow} + (1-\alpha)(1-i_0)F_{sw} \tag{2}$$

where q is the energy per unit volume required to melt the surface material (either snow or ice), and h is the thickness. F_s and F_l are the sensible and latent heat flux, $F_{L\downarrow}$ and $F_{L\uparrow}$ the incoming and outgoing longwave radiation, and F_{sw} the incoming shortwave radiation. The parameters α and i_0 represent, respectively, the shortwave albedo and the fraction of absorbed shortwave radiation that penetrates the ice. The term $(1-\alpha)(1-i_0)F_{sw}$ represents the portion of solar radiation absorbed in the surface layer, contributing directly to ice heating or melting. A similar formulation governs the energy balance at the bottom of the ice, accounting for oceanic heat fluxes.

MUSE-I includes two **radiative transfer methods** to compute surface albedo and shortwave radiative fluxes: the \ccsm3" method and a multiple scattering radiative transfer scheme based on the Delta-Eddington formulation [3]. The \ccsm3" is a parametric radiative scheme where the albedo depends on the temperature, ice/snow thickness and the spectral composition of incoming solar radiation; it's relatively simple and computationally efficient. The Delta-Eddington scheme is a two-stream approximation that simplifies the full radiative transfer equation by considering only the upward and downward components of radiative flux, rather than resolving the full angular distribution. This approach explicitly models the scattering and absorption of shortwave radiation within the ice and snow layers, taking into account key physical properties such as grain size and stratification. The model uses prescribed inherent optical properties for snow and sea ice, such as extinction coefficient and single scattering albedo, based on physical measurements. From these, the scheme computes the apparent optical properties (i.e., the reflected, absorbed, and transmitted components of shortwave radiation) for each layer of snow and ice in a physically consistent manner.

The equation governing the **heat transfer in the vertical direction**, which describes the rate of change in temperature inside the ice T within the ice layer i over time, can follow the formulation introduced in [1] in which the ice temperature is treated prognostically while the sea ice salinity profile is assumed temporally constant:

$$\rho_i c_i \frac{\partial T_i}{\partial t} = \frac{\partial}{\partial z}(k_i \frac{\partial T_i}{\partial z}) - \frac{\partial}{\partial z}[I_{pen}(z)] \tag{3}$$

where ρ_i is the sea ice density, c_i the specific heat of sea ice, k_i its (effective) thermal conductivity, and I_{pen} is the flux of solar radiation penetrating to depth z (downward positive) that depends on the radiation scheme used. Heat capacity and conductivity depend on both ice salinity and temperature. Once Equation 3 is solved, the ice and snow growth and melting rates at the ocean and atmosphere interfaces are computed to update their volume. The MUSE-I thermodynamics module includes two alternative formulations. The first is the simpler zero-layer sea ice and snow scheme [40], which does not explicitly resolve internal temperature variations within the ice. Instead, it assumes a linear temperature profile through the ice and snow and solves only for the surface temperature. The second is the mushy-layer formulation [42], a more physically detailed approach to model sea ice thermodynamics, especially during the freezing and melting processes. It considers sea ice as a porous mixture of pure ice crystals and liquid brine (distributed within a permeable matrix) whose structure evolves with changes in temperature and salinity. Salinity is treated as a prognostic variable, allowing the model to track its evolution over time. As ice forms, salt is partially rejected into the brine; during melting, brines may drain or mix with the ocean. These processes directly affect the enthalpy (total energy content) of the ice, since both temperature and salinity influence the phase (solid/liquid) state of the medium. The enthalpy is expressed as

$$q = \phi q_{\text{br}} + (1-\phi) q_i = \phi \rho_w c_w T + (1-\phi)(\rho_i c_i T - \rho_i L_0) \tag{4}$$

where ρ_w and c_w are the density and specific heat of seawater, ρ_i and c_i are the density and specific heat of ice, and L_0 is the latent heat of fusion for pure ice. Melting at the top surface is governed by

$$q\,\delta h = \begin{cases} (F_0 - F_{ct})\,\Delta t_0 & \text{if } F_0 > F_{ct} \\ 0 & \text{otherwise} \end{cases} \tag{5}$$

with δh the corresponding change in thickness. If the surface layer melts completely, any remaining energy is used to melt the underlying layers. Once both ice and snow are fully melted, excess energy is transferred to the ocean mixed layer. While ice cannot grow at the top surface through conductive fluxes, snow-ice formation can still occur. New snowfall is added at the end of the thermodynamic time step. Growth and melting at the bottom ice surface are given by the energy balance

$$q\,\delta h = (F_{cb} - F_{bot})\,\Delta t \tag{6}$$

Positive values correspond to ice growth, while negative values indicate melting. Δt is the time step. F_{cb} is the conductive heat flux at the bottom of the ice:

$$F_{cb} = \frac{K_{i,N+1}}{\Delta h_i}(T_i^N - T_f) \tag{7}$$

where $K_{i,N+1}$ is the thermal conductivity at the interface between the bottom ice layer and the ocean, Δh_i is the thickness of the bottom ice layer, T_i^N is the temperature at the bottom ice layer, and T_f is the freezing temperature of seawater. F_{bot} is the downward heat flux from the ice to the ocean, given by

$$F_{bot} = -\rho_w c_w c_h u^*(T_w - T_f) \tag{8}$$

c_h is a heat transfer coefficient, T_w and T_f are the sea surface temperature and freezing point, respectively, and u^* the friction velocity computed as $\sqrt{\frac{|\vec{\tau}_w|}{\rho_w}}$, $\vec{\tau}_w$ being the wind stress at the ice-ocean interface. A minimum value for u^* is applied to prevent unrealistically low fluxes. If ice is melting at the bottom surface, q in Equation (6) represents the enthalpy of the bottom ice layer. If ice is growing, it is the enthalpy of new ice, which is added to the bottom layer.

The presence of melt ponds on the sea ice surface strongly affects the exchanges between sea ice and the atmosphere in the spring/summer months. They allow for more incoming shortwave radiation absorption than bare ice and snow, with important implications on the energy and mass budget of the sea ice system. We included, in the thermodynamics module in MUSE-I, two widely used prognostic **melt pond parametrisations**, the topographic scheme [14] and the level-ice formulation [21], which both simulate the formation, evolution, and impact of melt ponds on the ice surface, influencing the overall ice-albedo feedback and energy balance. It is important to note that all of them require the use of the delta-Eddington radiation method for the explicit treatment of radiative transfer through melt ponds. In contrast, the ccsm3 shortwave scheme incorporates melt pond effects implicitly by adjusting the surface albedo based on surface conditions. For each parametrisation, the melt pond evolution is determined by the meltwater volume ΔV_{melt} produced at each time step t of the numerical model that can be added to the melt pond liquid volume at the following time step $t+1$. This volume is computed based on

$$\Delta V_{melt} = \frac{r}{\rho_w}(\rho_i \Delta h_i + \rho_s \Delta h_s + F_{rain} \Delta t) a_i \tag{9}$$

where r is the fraction of the total meltwater produced that is added to the ponds, ρ_i and ρ_s are ice and snow density, Δt is the time step size, Δh_i and Δh_s are the thickness of melted ice and snow and F_{rain} is the rainfall rate. The topographic scheme is based on the idea that meltwater accumulates in the lowest areas of the ice surface. Since our model (as originally Icepack) do not explicitly resolve surface topography, the ITD is decomposed into a surface height and basal depth relative to sea level; then, meltwater is assigned to the ice with the lowest surface elevations. The level-ice formulation also includes gravitational effects, but in a simplified way in which ponds are allowed to form only on undeformed (level) ice within each thickness category. In both cases, melt pond water can refreeze, reducing the effective pond area, or can drain vertically to the ocean, depending on sea ice permeability.

2.2 SEA ICE DYNAMICS

Sea ice dynamics refers to the study of the movement and deformation of sea ice under the influence of external forces. Unlike thermodynamics, which governs the growth and melt of sea ice, dynamics is concerned with how ice drifts, deforms, and interacts mechanically. It plays a critical role in determining the spatial distribution of sea ice, its thickness, and its concentration, especially in regions with strong winds, ocean currents, and interactions between ice floes.

MUSE-I describes the ice motion by solving the $\mathbf{momentum\ balance\ equation}$, which governs the horizontal motion of the ice and accounts for the balance between external forcing (such as wind and ocean drag) and internal ice stress resulting from deformation processes like ridging and rafting. Sea ice is typically treated as a two-dimensional, vertically-integrated continuum, which allows its large-scale motion to be modelled without resolving the full 3D physics. The momentum equation is expressed as

$$m\frac{\partial u}{\partial t} = \underbrace{\vec{\tau}_a}_{\text{atmospheric stress}} + \underbrace{\vec{\tau}_w}_{\text{oceanic stress}} + \underbrace{\vec{\tau}_b}_{\text{seabed stress}} - \underbrace{\hat{k} \times mf\mathbf{u}}_{\text{Coriolis term}} - \underbrace{mg\nabla H_o}_{\text{ocean tilt}} + \underbrace{\nabla \cdot \sigma}_{\text{internal stress}} \tag{10}$$

where m represents the mass of sea ice (and snow) per unit area, $\mathbf{u}$ is the sea ice velocity vector. On the right side, $\boldsymbol{\tau}_a$ and $\boldsymbol{\tau}_w$ are, respectively, the wind stress at the ice-atmosphere interface and the ocean stress at the ice-ocean interface. The two following stresses are, respectively, due to the Coriolis effect (f and $\mathbf{k}$ are respectively the Coriolis parameter and the vertical unit vector) and pressure gradients associated with the tilt of the ocean surface. The divergence of the two-dimensional stress tensor, $\nabla \cdot \sigma$ represents the internal stress of the ice. This equation describes how sea ice accelerates and deforms in response to both internal stresses and external forces over time. We close the system by modelling the mechanical behaviour of the ice, such as deformation and fracture, through a rheological model that relates the internal stress tensor σ to the strain rates within the ice. In MUSE-I, the internal stresses are computed assuming the Elastic-Viscous-Plastic (EVP) rheology ([20, 22]), widely used in sea ice models as a numerical approximation of the more physically grounded Viscous-Plastic formulation (VP, [18]). In VP, internal stresses are determined by a non-linear constitutive law that relates stress to strain rate through a plastic yield curve. This equation is theoretically robust, but it requires iterative, implicit solvers that involve numerous sub-time-step iterations to achieve satisfactory numerical convergence when computing the internal ice stress. The EVP formulation circumvents this limitation by introducing a pseudo-elastic component that relaxes the stress toward the viscous-plastic solution over a short time scale, significantly reducing computational costs and gaining numerical efficiency by permitting a fully explicit implementation with an acceptably long time step. In EVP, the internal stress tensor evolves according to

$$\frac{\partial \sigma_{ij}}{\partial t} + \frac{1}{T_e}\left(\sigma_{ij} - \sigma_{ij}^{\mathrm{VP}}\right) = 0 \tag{11}$$

where σ_{ij} is the current stress tensor, $\sigma_{ij}^{\mathrm{VP}}$ is the target stress tensor defined by the VP constitutive law, and T_e is the elastic relaxation timescale (that determines the timescale of transition from elastic behaviour to the VP rheology). This equation means the stress tensor σ_{ij} relaxes toward the VP solution $\boldsymbol{\sigma}_{vp}$ on timescale T_e. The VP constitutive law defines how internal stress σ_{ij} depends on the strain-rate tensor $\dot{\varepsilon}_{ij}$, via the bulk viscosity ζ and shear viscosity η (cf. [27, 18]):

$$\sigma_{ij} = 2\eta\, \dot{\varepsilon}_{ij} + (\zeta - \eta)\, \dot{\varepsilon}_{kk}\, \delta_{ij} - \frac{P}{2}\, \delta_{ij} \tag{12}$$

with the strain rate tensor computed from the velocity field $\dot{\varepsilon}_{ij} = \frac{1}{2}\left(\frac{\partial u_i}{\partial x_j} + \frac{\partial u_j}{\partial x_i}\right)$ the rate-of-deformation tensor. δ_{ij} is the Kronecker delta, and P represents the sea ice strength, which quantifies the internal pressure the ice pack can sustain before deforming plastically. Two parameterisations are implemented for its computation. Hibler (1979) is based on empirical scaling in which P is a function only of average ice concentration (A) and thickness (h) per grid cell

$$P = P^* h \, e^{-C(1-A)} \tag{13a}$$

where P^* and C are empirical constants, h is the ice thickness (m). Physically, P is large for thick, compact ice and smaller for thinner or fragmented ice. Rothrock (1975) considers P as a function of the ITD in each grid cell, and the energy required to form pressure ridges following

$$P = C_f \cdot C_p \int_0^\infty h^2 \cdot g(h) \, dh \tag{13b}$$

with C_f a friction/efficiency coefficient (dimensionless), C_p a physical constant that includes gravity and ice/water densities, and $\omega_r(h)$ represents the effective sea-ice volume change for each thickness class due to mechanical redistribution. P increases with the presence of thicker ice due to the h^2 term in the integral expression. It depends on the amount of ice volume available for ridging, and it incorporates mechanical energy considerations rather than relying solely on empirical fitting. Although EVP introduces some sensitivity to the choice of elastic time step and damping parameters, it is a practical and effective choice for large-scale sea ice simulations. It is particularly well-suited for parallel computing and provides a practical approximation of the VP solution with sufficient accuracy for large-scale sea ice modelling. Being the EVP formulation explicit in time, it requires sub-cycling within each external time step of the sea ice or ocean circulation model. The momentum equation and stress calculation are stepped forward in time using a reduced sub-cycling time step $\Delta t_{\mathrm{EVP}} = \frac{\Delta t}{N_{\mathrm{EVP}}}$, where Δt is the external model time step and N_{EVP} is the number of sub-cycles. To ensure numerical stability for the CFL condition, the external time step Δt has to scale proportionally with the mesh resolution. This implies that higher-resolution simulations require more EVP sub-cycles, which in turn increases the overall computational cost. To eliminate the dependency between the subcycling time step and numerical stability constraints present in the standard EVP formulation, we adopted the approach proposed by Bouillon et al. (2013) [2] and Kimmritz et al. (2015) [24], which introduces a modified EVP (mEVP) method where the subcycling procedure is fully decoupled from the physical time stepping. Two constant sub-cycling parameters α and β are introduced to control the stability and convergence of the pseudo-time iteration used to solve the sea ice momentum and internal stress equations. Specifically, α regulates the relaxation of the velocity field, while β governs the adjustment of internal stresses. The parameters are typically set to values of order $\mathcal{O}(10^2)$ (although they may vary depending on the resolution, time step, and dynamic characteristics of the simulation), with N_{EVP} required to exceed both α and β. The current MUSE-I simulation at approximately 25 km requires $N_{\mathrm{EVP}} > 100$.

Once the ice velocity field is computed from the momentum balance equations, the **advection scheme** is used to transport tracers such as ice concentration, ice thickness, snow depth, and enthalpy across the model grid as the ice drifts. This scheme is crucial for accurately capturing the spatial and temporal evolution of sea ice properties. For a generic tracer ψ, this equation is

$$\frac{\partial \psi}{\partial t} + \nabla \cdot (\mathbf{u}\psi) = 0 \tag{14}$$

MUSE-I adopts the Finite Element-Flux Corrected Transport (FE-FCT) scheme by [29], designed to solve advection-dominated equations with high accuracy while maintaining the sharpness of interfaces (e.g., ice edges) and preventing non-physical oscillations in tracers is crucial. This scheme proceeds in two steps, first a high-order finite element (FE) update computed to achieve greater spatial accuracy, and then a flux correction transport (FCT) based on the local behaviour of the solution to enforce desirable properties such as positivity and boundedness, for example ensuring that the ice area fraction remains between 0 and 1. The FE method provides spatial flexibility and high-order accuracy for solving partial differential equations on unstructured grids, allowing smooth representation of fields like ice concentration or thickness, even in complex geometries. The FCT acts as a stabilisation mechanism by blending a high-order solution (which may introduce non-physical oscillations) with a low-order, monotonic solution (which may be overly diffusive). The blending is controlled by flux limiters, which identify and mitigate numerical artefacts such as spurious oscillations while preserving as much of the high-order accuracy as possible.

2.3 MODEL INFRASTRUCTURE

Coupling with the ocean. MUSE-I is defined as a collection of driver routines external to the ocean model, which are invoked as needed. During the initialisation, these drivers are called to build the sea ice state and to define the sea ice parameters, whereas the sea ice time-stepping routines are integrated into the iterative process of the ocean model. Specifically, sea ice calculations are performed after the progression of ocean momentum, free surface elevation, and tracer fields such as temperature and salinity. At each time step, MUSE-I receives atmospheric and oceanic boundary conditions that are used to evolve the sea ice state. The required atmospheric fields, namely the 2-meter air temperature, 2-meter humidity, 10-meter winds, incoming shortwave and longwave radiation, and both solid and liquid precipitation, are passed directly from the ocean component to the sea ice model, avoiding the need to read them from external files. The oceanic forcing consists of sea surface temperature, sea surface salinity, sea surface height, and ocean currents.

MUSE-I is not currently coupled with an atmospheric model, so it exchanges sea ice physical quantities only with the ocean model, specifically sea ice concentration, ice-to-ocean freshwater and heat fluxes, and ice-to-ocean surface stress, ensuring consistent coupling of interphase processes. It is worth mentioning that the salinity fluxes from the ice to the ocean are inferred from the freshwater budget, assuming a constant salinity profile in the ice.

In their default options, the ocean and sea ice models handle air-sea and air-ice interactions using different bulk formulations. The ocean model currently adopts the ECMWF bulk formulation [9], incorporating cool-skin and warm-layer parametrisations based on [46] and [12], respectively. In contrast, the sea ice component in this version uses the latest NCAR bulk formulas [26], consistent with the original Icepack implementation. The NCAR formulation, retained for development purposes, might be used to operate MUSE-I in stand-alone mode, where the bulk scheme must independently handle the full air-ice interface without relying on coupling with the ocean model. Nonetheless, the ice-side bulk formulation remains modular and can be further customised depending on the ocean model configuration.

The code updates the sea ice state by following a structured sequence of steps, as outlined in [45]. Initially, after receiving input fields from the ocean model, MUSE-I advances the thermodynamic state of the ice, updating its internal temperature and salinity through the thermodynamic routines, which account for processes such as heat conduction, brine dynamics, and phase changes within the ice. Next, the momentum equation is integrated to compute the sea ice velocity field, with the rheology EVP solver to represent the internal stresses and deformation. Once the ice velocity is calculated, it is used by the FCT scheme to advect sea ice properties, ensuring stable and accurate transport without introducing spurious oscillations. Then, the model applies mechanical redistribution routines, which reshape the internal ice thickness distribution. Finally, the radiation scheme is updated to account for changes in surface albedo and energy balance, before the revised sea ice state is exchanged with the ocean model.

Numerical discretisation. All sea ice variables are discretised on an Arakawa A-grid where both scalar and vector quantities are defined at the mesh nodes. This differs from the B-grid discretisation used in the ocean model, where velocities are located on the cell elements and scalar tracers (such as temperature and salinity) reside at the nodes. To ensure compatibility and seamless coupling between the sea ice and ocean components, interpolation from the A-grid to the B-grid is applied to sea ice velocity fields when transferring information to the ocean (Figure 1). Conversely, the ocean surface velocities are interpolated from the B-grid to the A-grid before being used in the sea ice model. These interpolations occur every time the coupling between the ocean and sea ice components occurs.

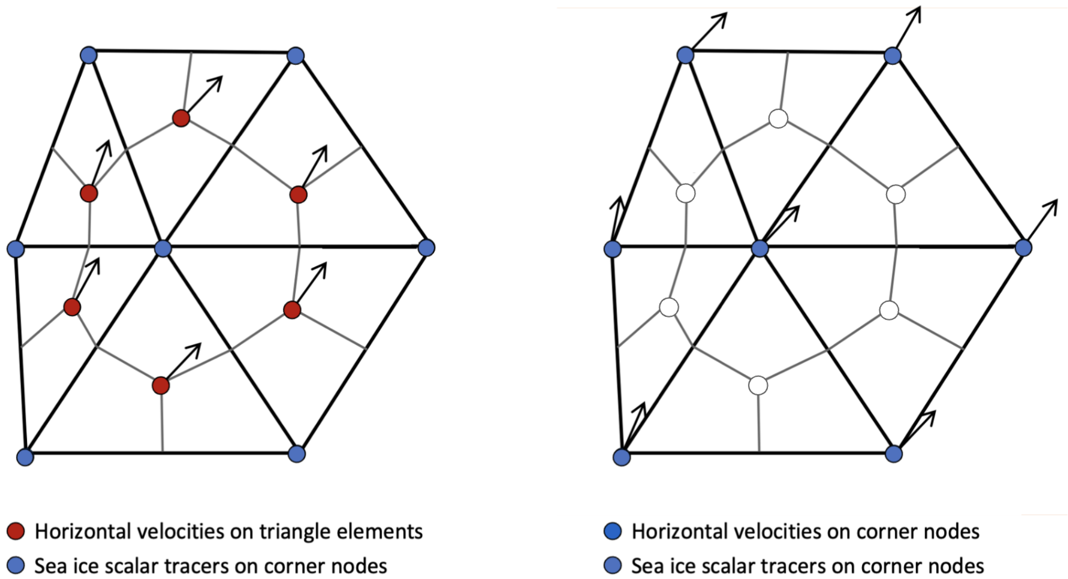

Figure 1. The Arakawa B-grid adopted for storing sea ice variables (left) and the Arakawa A-grid used for sea ice dynamics computation (right).

2.4 INPUT/OUTPUT CAPABILITIES

The Input/Output (I/O) capabilities of MUSE-I rely on the infrastructure built for the ocean component. The implementation permits the output of all prognostic and diagnostic variables describing the sea ice state with a high degree of flexibility. This is crucial for a comprehensive evaluation of the modelled sea ice and for taking advantage of the large number of tracers implemented. Diagnostic output is not limited to grid-cell averaged quantities, but is also available for single ITD classes, FSD classes, and single vertical layers.

In practice, the diagnostic outputs from the sea ice component are handled by a third-party library: the XML Input/Output Server (XIOS), an asynchronous MPI parallel I/O server used by Earth system models to avoid process contentions [4, 44]. XIOS runs alongside the MUSE ocean/ice code and offers high performance to achieve model output scalability. The output fields can be the result of in-line post-processing operations (both temporal and spatial) that use internal parallel workflow and dataflow. MUSE output consists of netCDF files that preserve the unstructured mesh of the model; they are flexibly controlled by external XML files adapted by the users, which allows easily changing the output configuration without recompiling the model code. XIOS is an open-source software and is licensed under the CeCILL license. The XIOS is made available with documentation and a user guide at `https://forge.ipsl.jussieu.fr/ioserver`.

MUSE-I has multiprocessor restart capabilities based on binary files. At restart time, the sea ice state for each model process is saved into a separate file from the ocean state, and subsequently read at the next initialisation of MUSE. When restart files are not provided, the sea ice state is initialised with a constant ITD distribution where the sea surface temperature (SST) is cold enough to allow sea ice to form (the default option sets the sea ice when initial SST $\leq -1.8^{o}$C).

3. MODEL SETUP AND EVALUATION FRAMEWORK

This section describes the configuration setup of the coupled ocean-sea ice model and presents a set of validation tests performed to assess the numerical stability and physical consistency of the implemented components. The setup features the integration of the thermodynamic sea ice module with the ocean model, driven by prescribed atmospheric forcing. It should be noted that these tests focus exclusively on the thermodynamic component of the sea ice code, as MPI parallelisation of the dynamic routines is still under development.

The MUSE-I is evaluated through multi-year global simulations, using the current default configuration of the ocean component as a baseline. The computational mesh comprises approximately 1.1 million horizontally triangular nodes and 72 vertical levels, prescribed via the ocean model namelist. The horizontal resolution ranges from 25 km at the equator to 6 km near the poles, while the vertical resolution spans from 2 m at the sea surface to 200 m in the deep ocean. Ocean and sea ice components share the same grid and MPI-based domain decomposition. The mesh is generated using the software JIGSAW-GEO [11] with the General Bathymetric Chart of the Oceans (GEBCO, [16]), which provides the ocean depth on a 15 arc-second interval grid. Bathymetric data are interpolated onto the MUSE-I grid using a bilinear method with a 0.15°radius. Minimum and maximum depths are set to 10 m and 6000 m, respectively.

A series of preliminary tests was carried out to assess the numerical stability and physical robustness of the implemented components and the newly added schemes, and to demonstrate that the thermodynamic module can run in 1D and 2D configurations, in stand-alone and coupled mode with the ocean model while receiving atmospheric forcing fields. These tests confirmed the model's ability to produce physically consistent results aligned with the underlying thermodynamic formulations.

3.1 SIMULATION 1: STABILITY OF THE THERMODYNAMIC MODULE

One of these tests, referred to as Simulation 1, is presented as a representative example. This is a long-term simulation, performed with the ocean component coupled to sea ice, designed to evaluate the stability of the thermodynamic module in a two-dimensional medium-complexity configuration. The setup features an ITD with five thickness classes and the BL99 thermodynamics with 4 + 1 vertical layers, and the radiative transfer based on the Delta-Eddington scheme. Sea ice initial conditions are described with a constant fixed thickness, where the presence of ice depends on the SST threshold. The simulation spans the period from January 2005 to August 2011, starting from an ocean at rest and initialised with temperature and salinity fields derived from the 2005-2014 climatology of the World Ocean Atlas 2023 [33]. Atmospheric forcing is applied hourly using ERA5 global reanalysis data [17], produced by the European Centre for Medium-Range Weather Forecasts (ECMWF), at a spatial resolution of 0.25°. Sea ice outputs are generated as daily averages. Given the simplified nature of the experiments, tidal forcing and river runoff (still under development in the ocean code) were deactivated to ensure tighter control of the simulated thermodynamic behaviour.

Figure 2 presents the time series of three key diagnostics commonly used to evaluate sea ice model performance: total sea ice area (SIA), spatially averaged sea ice thickness (SIT), and spatially averaged snow depth. The SIA is computed by integrating sea ice concentration across the entire model domain, weighted by the area of each grid cell. Both the Arctic and Antarctic regions are shown. The multi-year continuity and absence of numerical instability suggest that the thermodynamic and coupling components are functioning as intended. SIA results (Fig. 2a) are consistent with the well-established seasonal cycle of SIA in both hemispheres, with opposite phases; they demonstrate that the model captures the expected seasonal behaviour and hemispheric asymmetry of ice coverage. The smoothness and regularity of the cycles also suggest a stable thermodynamic response over multiple years. In the Arctic, SIA reaches its annual maximum around March, corresponding to the end of the freezing season, and its minimum around September, at the end of summer melt. The amplitude of the seasonal cycle remains relatively stable over the simulation period, with SIA varying between approximately 5 and 15 million km^2. Compared to the Arctic, the Antarctic seasonal variability is more pronounced, with minima similar to the Arctic one during the austral summer (around February) and maxima of over 20 million km^2 during the winter months. A more persistent Arctic sea ice cover with moderate seasonal variability, and a more extensive but highly seasonal Antarctic cover, consistent with observed climatological behaviour. This strong contrast reflects the predominantly seasonal nature of Antarctic sea ice, which forms and melts completely in large peripheral areas each year.

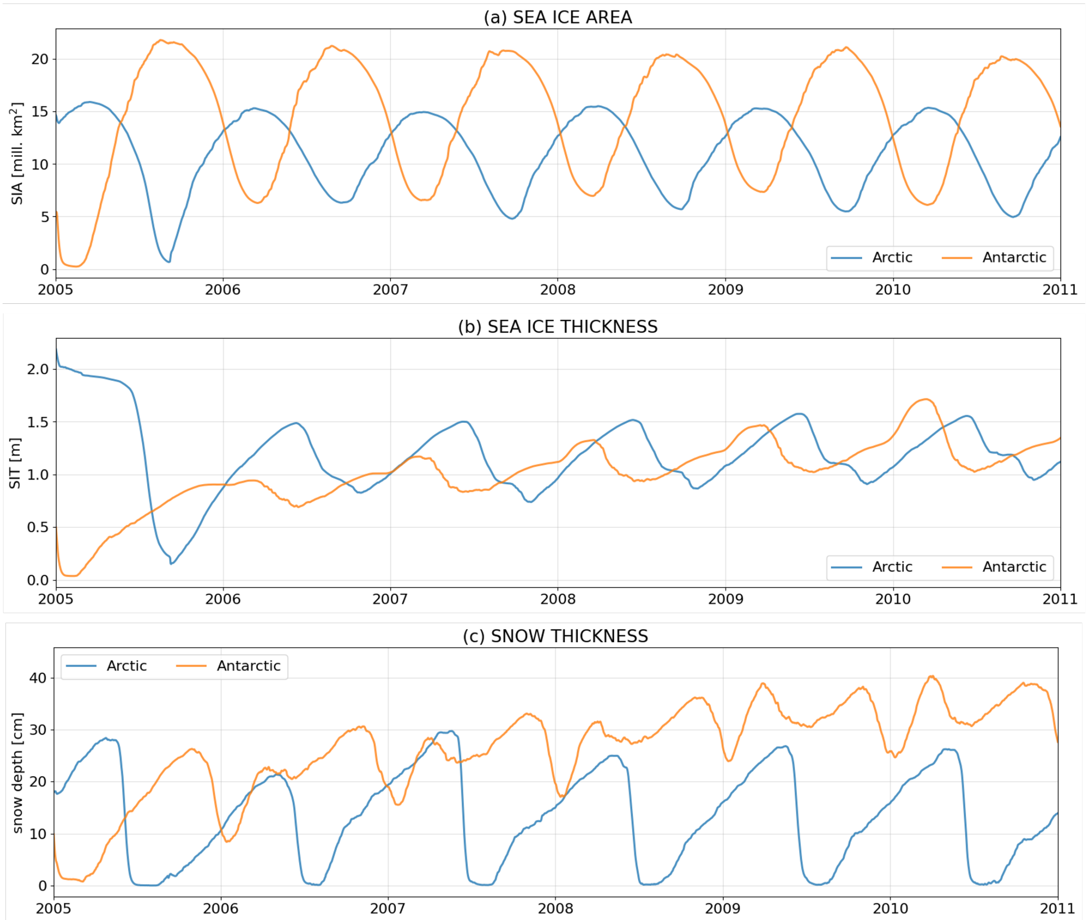

Figure 2. Time series of total sea ice area (a), spatially-averaged sea ice thickness (b), and spatially-averaged snow thickness (c) in Arctic (blue line) and Antarctic (orange line) regions.

The time series of SIT (Fig. 2b) requires a longer time (mainly in the Southern Ocean) to stabilise and reach *equilibrium*, as it reflects the cumulative effects of thermodynamic growth and melt, ocean-ice heat exchange, and snow accumulation over multiple seasons. This behaviour is also influenced by the sea ice initialisation, which derives ice presence from ocean surface temperature and relies on a default distribution function to allocate ice across the ITD categories. Unlike sea ice area, which responds more directly to atmospheric forcing on shorter timescales, thickness integrates slower processes and therefore adjusts more gradually. It is important to note that sea ice dynamics are not activated in this simulation; hence, the ice does not drift or deform. As a result, the SIT evolution solely reflects the effect of vertical processes, such as surface and basal melting/freezing and snow accumulation, without contributions from mechanical redistribution. This helps explain the similarity in the amplitude and range of the seasonal SIT cycle observed in both hemispheres.

In the Arctic, SIT reaches its maximum in spring, when thick, consolidated ice has accumulated over the winter months. Although the experiments are relatively simplified, the thermodynamic response to oceanic and atmospheric forcing is consistent with the Arctic SIT time variability presented in [6], based on both observational data and ocean-ice reanalyses. In contrast, the Antarctic exhibits its highest average SIT during summer, when thin marginal ice has melted away and only the thicker, more stable inner pack ice remains, increasing the spatially averaged thickness. In the Southern Hemisphere, thermodynamic-only simulations are not able to accurately reproduce summer sea ice melting, resulting, over time, in an overestimation of sea ice thickness. The spatially averaged snow thickness over sea ice (Fig. 2c) displays a clear seasonal cycle in both hemispheres, but with notable differences in amplitude, timing, and accumulation patterns. In the Arctic, snow depth exhibits a pronounced seasonal signal, increasing steadily during autumn and winter, reaching peak values around March-April, and rapidly decreasing during the melt season in late spring and summer. The cycle is strongly asymmetric, with slow accumulation and rapid ablation, consistent with the seasonal snowfall and melt processes. In contrast, the Antarctic shows higher average snow depth throughout the period, with more gradual and continuous accumulation and less abrupt melt phases. Seasonal peaks are broader and occur later in the year, typically around September-October, when sea ice extent is also near its maximum. The observed behaviour can be explained by the combination of weaker surface melting relative to the Arctic and the greater influence of the absence of mechanical snow redistribution by ice motion in the Southern Ocean.

The time series of aggregate sea ice and snow thickness (in Fig. 3) illustrates the evolution of the total vertical extent of the ice-snow column for the Arctic and Antarctic regions. The shaded areas indicate the combined vertical extent of the ice-snow column. The plot highlights the distinct timing of the seasonal cycles of sea ice and snow. In the Arctic, the annual minimum depth is reached first by the snow layer, followed later by the sea ice. A similar pattern is observed for the maximum: the ice thickness reaches its peak after the snow depth has already begun to decline. In the Antarctic region, the combined ice-snow column exhibits a comparable behaviour, although it is more difficult to interpret due to the ongoing increasing trends in both sea ice and snow thickness.

The accuracy of the model in representing the spatial distribution of monthly averaged sea ice concentration, ice thickness, and sea ice surface temperature in the Arctic is illustrated in Figure 4, which shows results at the late freezing season and the late melting season. In March, the consolidated pack ice, characterised by sea ice concentration above 80%, covers nearly the entire Arctic domain and extends both in the Pacific and Atlantic Oceans (Fig. 4a). Responding to oceanic and atmospheric conditions, the thermodynamic module is able to produce ice also in regions such as the North Sea, Hudson Bay, and the Sea of Japan. In summer, the model responds to the atmospheric warming and even more to the enhanced oceanic heat transport into the Arctic Basin by restricting sea ice to the central polar cap while allowing extensive melt over the Eurasian sector and the Siberian shelf seas (Fig. 4b).

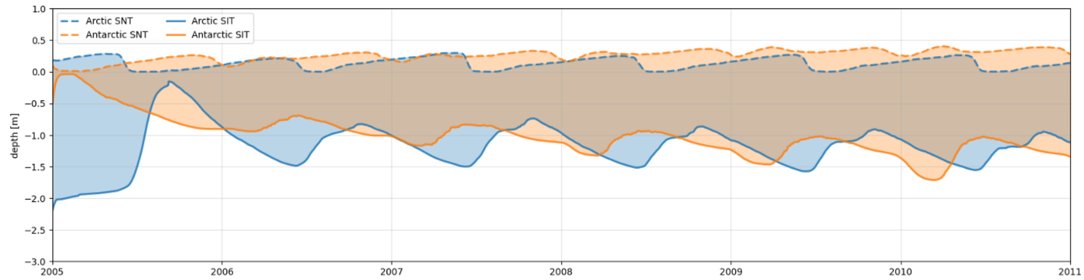

Figure 3. Time series of the aggregate sea ice (bold) and snow (dashed) thickness for Arctic (blue) and Antarctic (orange). Shadings indicate the overall depth.

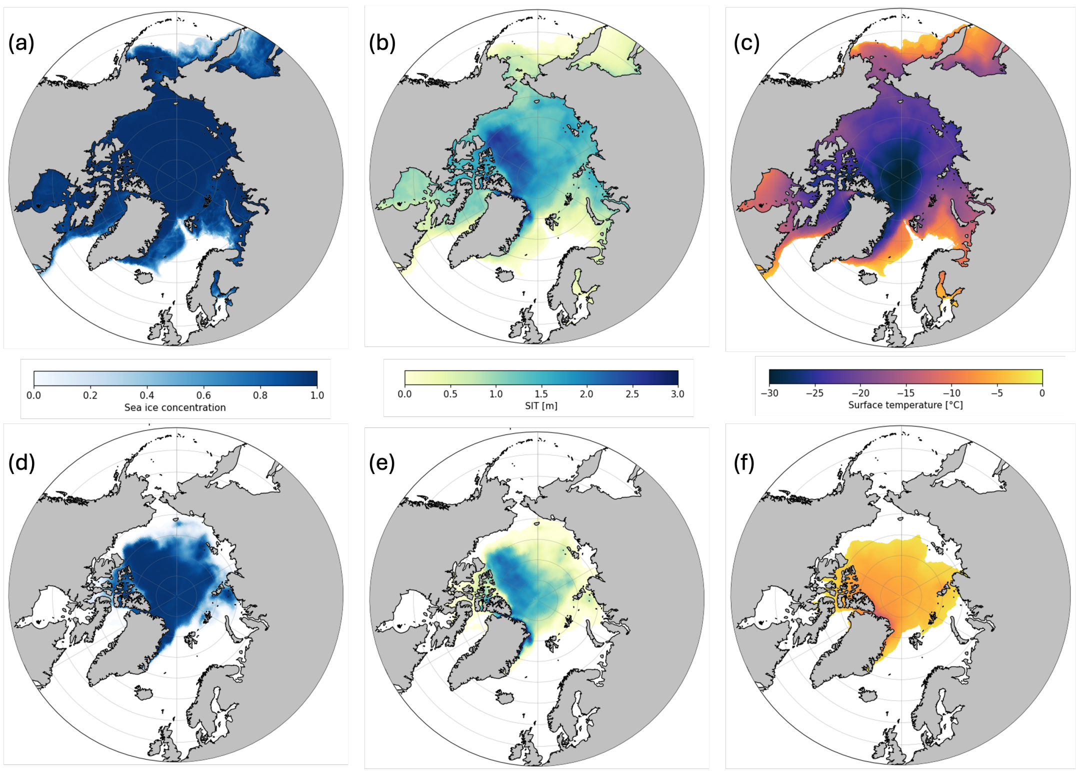

Figure 4. Spatial distribution of monthly averaged Arctic sea ice concentration (a, d), thickness (b, e), and sea ice surface temperature (c, f) for March (top row) and September (bottom row) 2011, the last simulated year.

The spatial patterns of sea ice thickness reasonably show thicker ice north of the Canadian

Archipelago and Greenland for the selected months (Figs. 4b,e), consistent with the presence of consolidated multi-year ice. In this region, ice thickness exceeds 2 m and gradually decreases toward the Siberian coasts, where it reaches approximately 1 m in winter and tends to vanish in summer. The absence of ice in the Eurasian marginal seas (Kara Sea, Laptev Sea, and the Siberian Shelf) due to the seasonal melting further indicates that the model responds effectively to the summer thermodynamic forcing. The persistence of thicker ice in the Canadian sector and the summer retreat in the Eurasian marginal seas are consistent with climatological observations; these simulated patterns arise solely from thermodynamic processes and are not influenced by large-scale ice drift or mechanical redistribution. Figures 4c and 4f display the spatial distribution of sea ice surface temperature in the same period. At the end of winter, surface temperatures are extremely low across the entire ice-covered domain, reaching below $-25\,^{\circ}$C in the central Arctic Basin. A clear latitudinal gradient is visible, with slightly warmer temperatures (around $-10\,^{\circ}$C to $-15\,^{\circ}$C) near the ice margins, especially in the Barents and Bering Seas. These patterns reflect the strong radiative cooling typical of late winter conditions and the absence of surface melting. After the melt season, sea ice surface temperatures are significantly higher and range between $-5\,^{\circ}$C and $0\,^{\circ}$C, with much of the remaining ice-covered area near the freezing point. This uniform warming of the surface is consistent with the seasonal melt and the thermodynamic response to peak atmospheric temperatures and oceanic heat input. The near-isothermal conditions across the remaining ice suggest the end of the melt season and a transition toward autumn freeze-up.

We omit a similar analysis for the Southern Ocean since the experiment setup prevents as the experimental setup prevents meaningful interpretation of the results. In Antarctica, sea ice conditions and variability are strongly governed by dynamic processes and respond more sensitively to both oceanic and atmospheric forcing. As a result, the spatial distribution of ice properties driven solely by thermodynamics, without ice dynamics, is challenging to interpret and does not closely resemble observed climatological distributions.

3.2 SIMULATION 2: HIGH-COMPLEXITY THERMODYNAMIC MODULE

The goal of this test is to evaluate the performance of MUSE-I under a high-complexity thermodynamic configuration, aimed at enhancing the physical realism of sea ice simulations. Simulation 2 incorporates advanced features such as prognostic salinity and melt pond representation, along with expanded diagnostic capabilities. The simulation covers the period from January 2009 to December 2011 and shares the same setup as Simulation 1 in terms of initial conditions, atmospheric forcing, and mesh resolution. However, it activates the "mushy" thermodynamics option, in which salinity is treated as a prognostic tracer alongside brine height, and includes the implementation of a topographic melt pond scheme. Still, this result should be interpreted with caution for comparison with observed fields, as the model configuration used here neglects sea ice dynamics.

Unlike prescribed salinity values as in Simulation 1, prognostic salinity evolves dynamically in response to freezing, melting, brine rejection, brine drainage, and flushing. This allows the model to more accurately represent the thermal properties of sea ice, as salinity directly affects both thermal conductivity and heat capacity. Also, simulating the distribution of brine within the ice can enable a better representation of vertical desalination and meltwater flushing during the summer. Figure 5 presents the spatial distribution of sea ice salinity (in practical salinity units, psu), as computed by the mushy-layer scheme, at the time of annual maximum and minimum extent at the end of integration, in both the Arctic and Antarctic regions. In March, surface salinity values are moderate over most of the Arctic pack ice (Fig. 5a), generally ranging from 4 to 8 psu, with higher salinities (10-12 psu) near the ice edge and marginal seas (e.g., Barents and Chukchi Seas). These values are consistent with older, more consolidated ice that has undergone brine expulsion and desalination (gravity drainage and brine expulsion) over time, and with young, recently formed ice, which tends to be saltier due to limited brine drainage. The Arctic sea ice salinity is generally lower and more uniform (mostly 2-6 psu) in September (Fig. 5b), especially in the central Arctic. This reflects the flushing and desalination processes occurring during the melt season, as meltwater dilutes surface brine pockets and facilitates brine drainage. This seasonal decline in surface salinity is consistent with observed processes in first-year and multi-year ice. In the Southern Ocean, sea ice is generally saltier than in the Arctic due to the large portion of newly formed sea ice (Figs. 5c,d). Salinity is relatively high across much of the region, particularly near the ice edge, reflecting active ice formation, and it decreases progressively toward higher latitudes. The salinity minima reproduced in the Weddell and Ross Seas clearly indicate the presence of stable, consolidated multi-year ice. In the late summer, a marked reduction in ice salinity is evident across much of the Antarctic ice cover, with widespread areas below 6 psu. This is consistent with intense summer melting and brine flushing. It is important to note that the thermohaline processes involved closely follow the seasonal cycle and do not require long-term adjustment to reach a physically consistent state, which justifies our use of a relatively short simulation. Even after only a few years of integration, the results behave as expected and are consistent with previous studies using the same parameterisation scheme, e.g. [8].

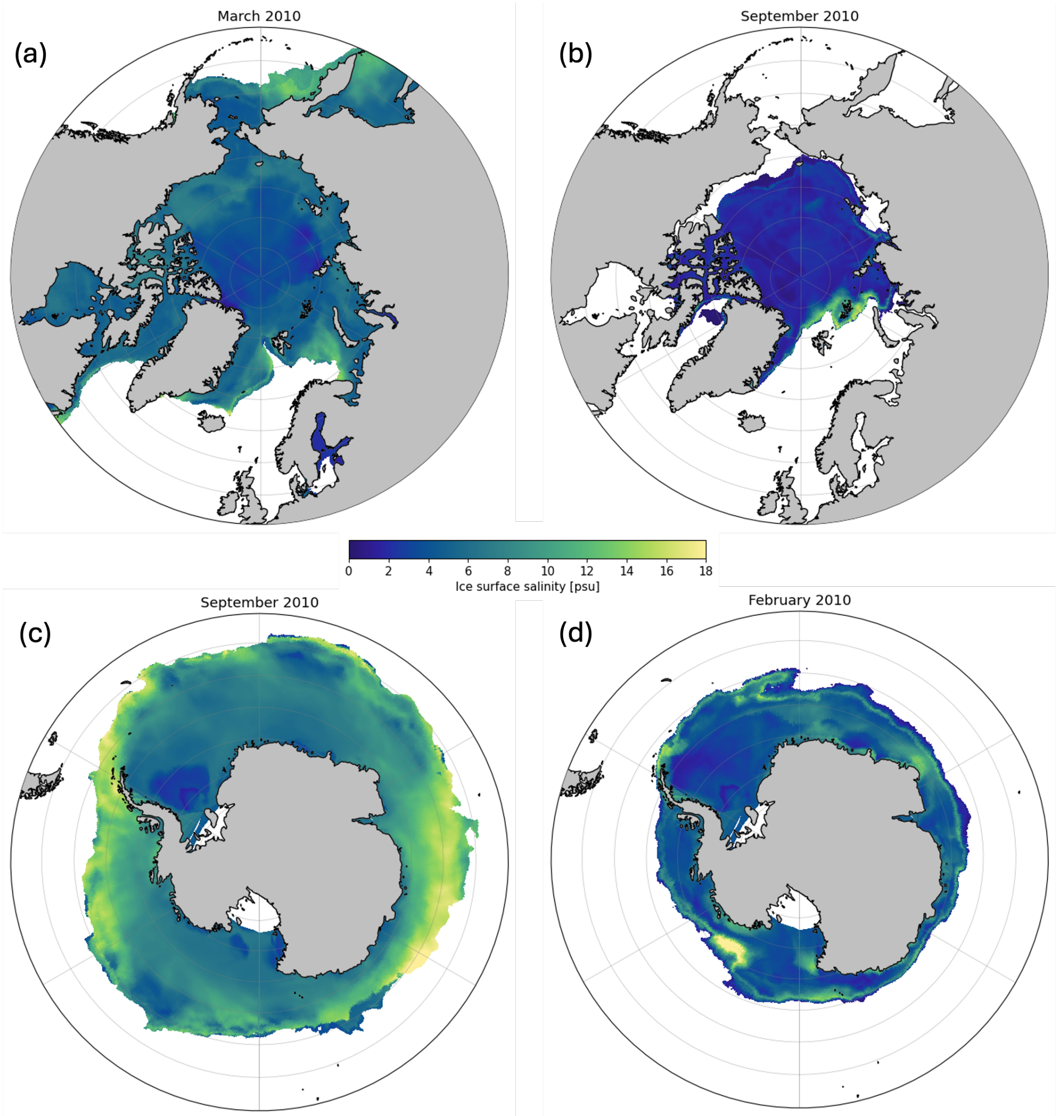

Figure 5. Maps of monthly averaged sea ice surface salinity at maximum (left panels) and minimum (right panels) of the seasonal cycle in the Arctic and Antarctic.

Sea ice salinity exhibits characteristic vertical profiles that evolve with ice age, as supported by observational evidence (e.g., [10]). Figure 6 demonstrates the ability of MUSE-I to simulate the vertical distribution and temporal evolution of ice salinity in both hemispheres. The figures present the time series of daily sea ice salinity averaged over the four vertical layers within the ice column, during the March-April period, corresponding to the onset of melting in the Arctic and the beginning of ice formation in Antarctica. The layers (1 to 4) correspond to increasing depth within the ice, with Layer 1 being the topmost and Layer 4 the bottommost. In the Arctic (Fig. 6a), salinity values are relatively low across all layers, with the bottom layer (Layer 4, red) around 2 psu and decreasing slightly over time. The upper layers remain between 0.8 and 1.4 psu. This suggests a regime dominated by thermodynamic equilibrium and brine drainage processes typical of older, thicker sea ice. The gradual reduction in salinity, particularly in deeper layers, reflects continued desalination as the ice remains relatively cold and consolidated late in the freezing season. In contrast, the formation phase in the Southern Ocean (Fig. 6b) shows significantly higher salinities, especially in the bottom layer (Layer 4), reaching over 14 psu in mid-April. Salinity increases over time in all layers, especially deeper ones. The higher values are typical of Antarctic younger ice, particularly during the early growth stages, when newly formed saline ice continues to accumulate. Both hemispheres show a realistic evolution of sea ice salinity, with the consistent evolution of the characteristic C-shaped vertical profile, higher salinity near the surface and base, and lower salinity in the interior.

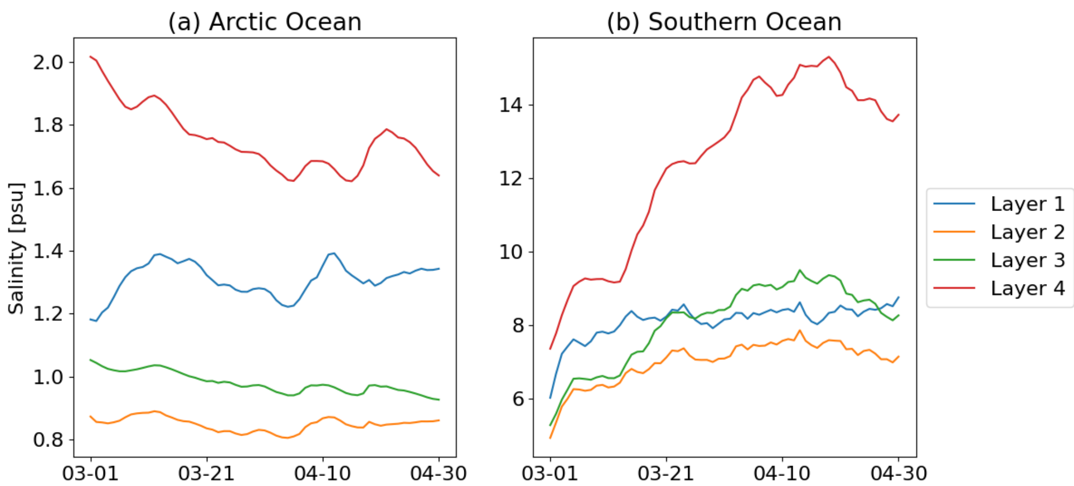

Figure 6. Time series of daily sea ice salinity averaged on sea ice layers in the Arctic (a) and Antarctic (b) regions in the March-April period.

Figure 7 shows the cumulative evolution of sea ice growth, melt, and freshwater flux in both hemispheres during Simulation 2, helping to assess how the thermodynamic module in MUSE-I responds to seasonal forcing. The total cumulative sea ice growth (in m) due to basal freezing is presented in Figure 7a,d for the two regions over the 3-year integration. Growth is strongly seasonal, with peaks in winter months, as expected. The Arctic shows slightly more intense cumulative growth, consistent with a more extensive and stable winter ice pack in a thermodynamic-only setting. The corresponding cumulative melt rates at the surface and bottom of ice are shown in Figures 7b,e. In the Arctic, surface melting dominates, especially during the summer peaks driven by strong atmospheric forcing. In contrast, in Antarctica, the dominant process, driven by oceanic heat transport, particularly in the Antarctic Circumpolar Current region. This difference in dominant melting mechanisms between hemispheres correctly highlights the sensitivity of the sea ice module to both atmospheric versus oceanic forcing, but we again note that this interpretation is constrained by the absence of sea ice dynamics routines. Figures 7c,f present total freshwater fluxes from sea ice melt into the ocean, expressed in kg/m²/s. Two clear summer maxima are visible in the Arctic, matching the melting periods and suggesting strong meltwater release during boreal summer, while in the Antarctic, flux is smoother but steadily positive, with less seasonal contrast (negative values may correspond to freezing events where brine is rejected into the ocean). This additional diagnostic information is intended to improve our ability to constrain the freshwater fluxes into the ocean within the coupling framework, which are critical for stratification, surface buoyancy, and mixed-layer processes.

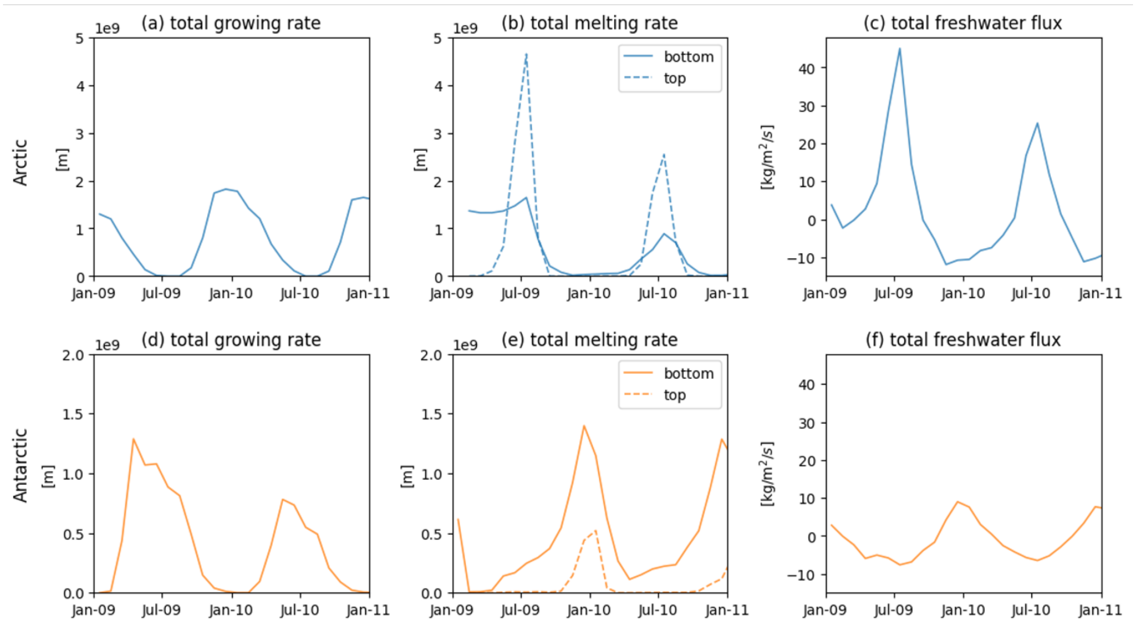

Figure 7. Seasonal evolution of tcumulative sea ice growth (a,d), melting rates separated into basal and surface contributions (b,e), and total freshwater flux from sea ice to the ocean (c,f) in the Arctic[1] (top row) and Antarctic (bottom row) for the period January 2009 to January 2011. Note the differing y-axis scales between hemispheres.

[1] The reader should note that the total melting rate for Arctic sea ice in January 2009 has been excluded from the time series to facilitate more accurate analysis.

Melt ponds significantly influence sea ice optical properties by reducing surface albedo, the fraction of incoming solar radiation reflected back into the atmosphere. As snow and surface ice melt, the resulting meltwater accumulates in small-scale surface depressions, forming darker ponds that lower the local albedo from snow-covered values (~0.85-0.90) to as low as 0.20-0.40. This enhanced absorption of solar radiation accelerates melting, establishing a positive feedback mechanism. Simulation 2 evaluates the most complex pond parameterisation implemented in MUSE-I, the topographic scheme (cf. [14]), in which the formation and evolution of melt ponds are governed by the small-scale topography of the ice surface, which controls both initial pond development and subsequent drainage pathways. The scheme distributes meltwater according to the prognostic ice thickness distribution (ITD), allowing water to accumulate in surface depressions until it overflows or drains. As surface melt advances, changes in topography due to subsidence or internal drainage enable ponds to deepen, merge, or drain vertically through cracks and macropores. In the Simulation 2 setup, the ITD evolves thermodynamically only, which limits the presence of thicker ice categories and, in turn, constrains the variability of topographic features that influence melt pond dynamics. This topographic scheme provides a physically consistent representation of melt pond area and volume across space and time, which is essential not only for accurately capturing albedo feedbacks but also for improving the coupling between sea ice thermodynamics and radiative transfer processes within the climate system.

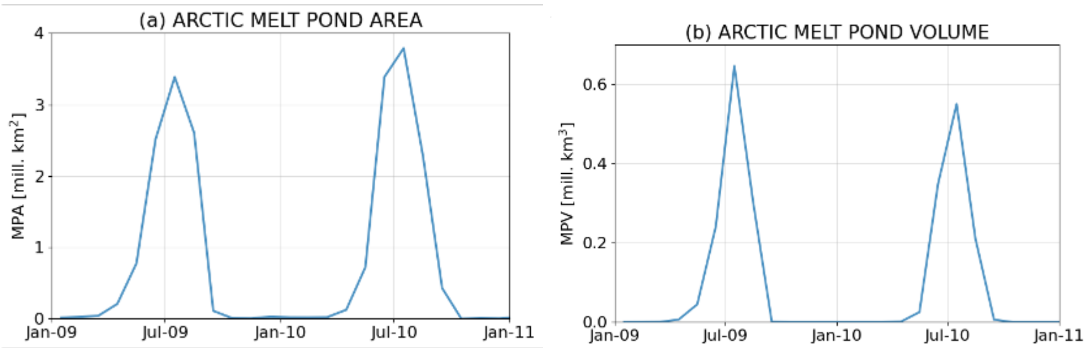

Figure 8. Monthly averaged melt pond area (a) and volume (b) for years 2009 and 2010.

Figure 8 presents the time series of monthly-averaged melt pond area (MPA) and volume (MPV) over the Arctic region for the years 2009 and 2010, providing insight into the seasonal evolution of surface meltwater on sea ice. In agreement with earlier studies (cf. [15, 47]), both parameters increase in spring toward summer to sharply disappear in early autumn. The melt pond area peaks around July, reaching over 3 million km^2 in 2010 (2.5 million km^2 from MODIS observations during 2000-2011, cf. [36]). This rise coincides with the peak of surface melting driven by increasing solar radiation and air temperatures. After the peak, the area rapidly declines as ponds drain or refreeze with the end of summer. The corresponding melt pond volume closely mirrors the area evolution but also reflects depth variations. Maximum volume values are observed just after the area peaks, suggesting that ponds continue to deepen slightly even after their spatial extent has begun to shrink. These results confirm that the melt pond scheme captures the typical Arctic seasonal cycle: a rapid onset of ponding in early summer, a well-defined maximum in mid-summer, and a complete drainage/refreezing by early autumn. The year-to-year consistency, with some variability in amplitude, suggests the model behaves robustly under repeated annual cycles.

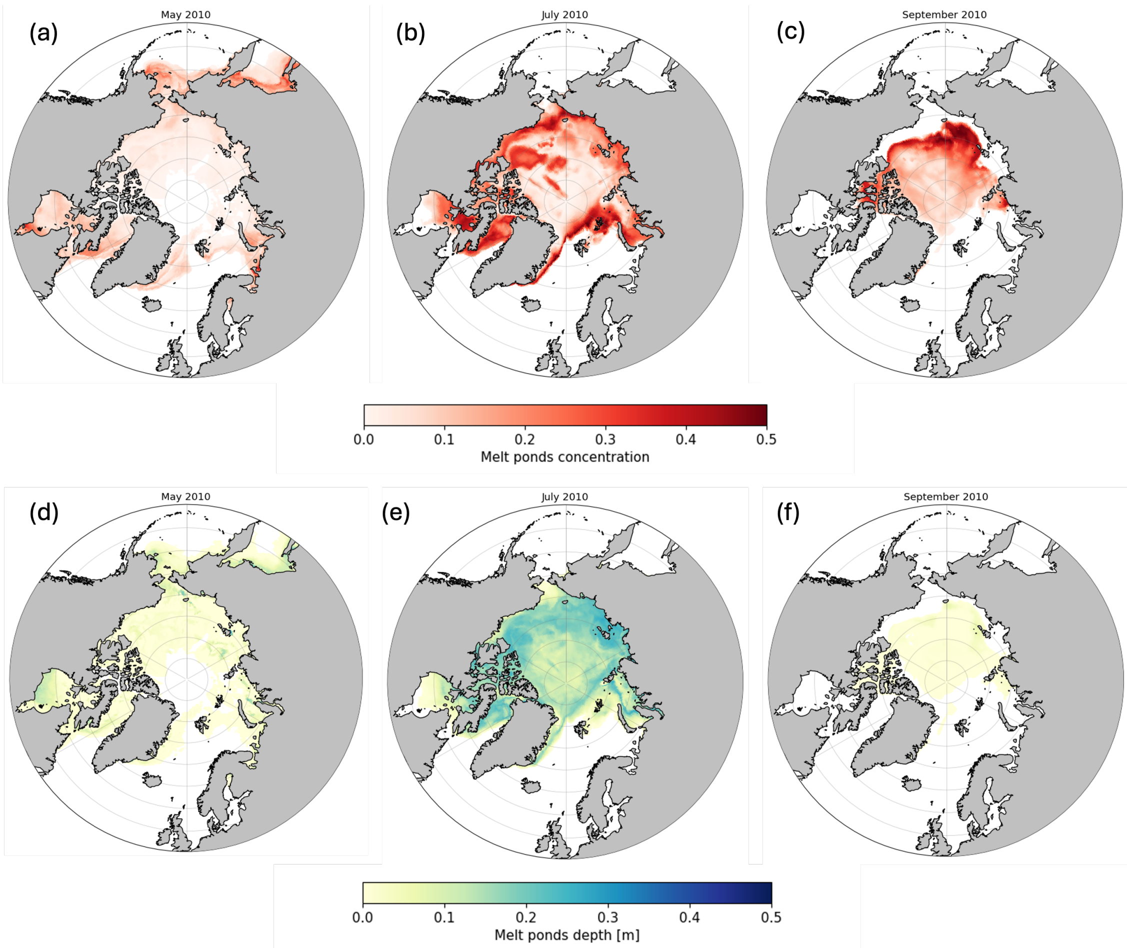

Figure 9. Monthly averaged melt pond concentration (a-c) and depth (d-f) for May, July, and September 2010, respectively.

Figure 9 presents the seasonal evolution of melt ponds during the summer melt season, showing the spatial distribution of melt pond concentration (in %) and melt pond depth (in m) over the Arctic for May, July, and September 2010. In May (Fig. 9a,d), melt pond concentration and depth are still relatively low and mostly confined to the southern and marginal parts of the Arctic sea ice cover, mostly absent in the central Arctic. This is the early stage of pond development, with isolated and shallow ponds beginning to form as surface melt initiates. In July (Fig. 9b,e), melt ponds reach their seasonal maximum in both concentration and depth, with a notable increase particularly in marginal ice zones such as the Greenland Sea, Kara Sea, Chukchi Sea, Canadian Archipelago, and Baffin Bay. While the spatial patterns of concentration and depth are generally consistent, local peaks in pond concentration do not always coincide with areas of greatest depth, which appear more spatially diffuse. Though the end of summer (Fig. 9c,f), high concentrations persist in some regions, like the East Siberian Sea and the Laptev Sea, while pond depth decreases uniformly across the Arctic, following late-season conditions, where surface melt slows, pond waters largely drain or may refreeze as air temperatures cool.

4. CONCLUSIONS

This report presents MUSE-I, the sea ice code developed at CMCC for application on unstructured meshes. The sea ice component is integrated into an ocean component currently under development, designed for global coastal applications at frontier spatial resolution. The report describes the MUSE-I physical formulation, the ocean-ice coupling strategy, and provides an initial evaluation of the vertical physics as introduced in the MUSE framework. MUSE-I incorporates state-of-the-art parameterisations for ice thermodynamic, dynamic, and mechanical processes, allowing it to simulate the evolution of sea ice in both polar open-ocean and coastal settings. The present assessment concentrates on the thermodynamic core, adapted from Icepack, whose individual parameterisation schemes were first tested in 1-D column configurations under various climate conditions to ensure numerical stability and physical consistency, and subsequently applied in global 2-D configurations. Here, we present two multi-year simulations that incorporate the most innovative thermo-haline vertical physics, tested at increasing complexity of thermo-haline processes. Simulation 1 employs a medium-complexity configuration comparable to that used in many climate models. Results demonstrate that MUSE-I can successfully reproduce the main seasonal cycles of ice and snow key properties in both hemispheres. Without active ice dynamics, the thermodynamic response remains physically consistent and aligns with climatological benchmarks, particularly in the Arctic, demonstrating the robustness of vertical energy and mass exchange mechanisms, including freezing and melting at the ice-ocean and ice-atmosphere interfaces. Performance in the Southern Ocean is more limited in this setup due to the absence of sea ice dynamics, which prevents a realistic representation of ice distribution and its response to oceanic and atmospheric forcing. Simulation 2 explored more advanced thermodynamic processes, including prognostic salinity via a mushy-layer scheme (treating ice as a porous ice-brine matrix) and a topographic melt-pond parameterisation. The mushy-layer scheme enables realistic simulations of spatial and vertical salinity patterns, consistent with observational evidence and previous studies. It properly captures ageing and desalination processes. The presence of melt ponds can enhance solar absorption and accelerate ice melt through a positive feedback mechanism that strongly influences the seasonal evolution and mass balance of sea ice. In MUSE-I, the topographic scheme successfully represents the seasonal evolution of pond coverage and depth, with peaks in summer months and near-zero values during winter, with a proper representation of drainage and refreezing features in late summer. These developments lay the groundwork for improved representations of albedo feedbacks and freshwater fluxes to the ocean. An ITD-based framework, modular thermodynamic tracers and multi-layer vertical structure enable MUSE-I to resolve key nonlinear feedbacks and structural ice complexity, such as those associated with variable thickness categories, energy storage, and internal brine dynamics. Future development will focus on activating and validating the sea ice dynamic core, improving coupling strategies with atmospheric and wave components, implementing floe size distribution schemes, and benchmarking model performance through intercomparisons with other established sea ice models. As part of future work, particular attention will be given to the activation and evaluation of the dynamic core and its computational performance. MUSE-I currently includes an EVP (and optionally mEVP) rheology solver for modelling sea ice dynamics. However, its numerical stability and accuracy depend strongly on the choice of relaxation time and damping parameters, which require careful calibration. The EVP approach may struggle to represent complex stress responses under high-deformation or anisotropic strain conditions, potentially limiting its ability to capture fine-scale mechanical features such as lead formation. Ongoing development will aim to address these limitations through testing, parameter tuning, and potentially exploring alternative rheologies. Overall, the preliminary results confirm that MUSE-I has the potential to become a flexible and robust sea ice modelling tool, capable of supporting both scientific research and operational applications within Earth system modelling frameworks. This initial evaluation demonstrates that its thermodynamic core and radiative transfer scheme perform reliably and consistently, even in the absence of full dynamic coupling. In concluding this report, we gratefully acknowledge the efforts of the CICE Consortium in developing and maintaining the Icepack thermodynamic module, which serves as the foundation of MUSE-I's sea ice thermodynamics. Icepack's modular and well-documented design has been instrumental in enabling seamless integration into the MUSE framework, offering a flexible and extensible suite of parameterisations. This design architecture not only supports a wide range of model complexities and configurations, but also promotes reproducibility, community-driven development, and interoperability with other ocean-ice systems.

In summary, MUSE-I represents a major step forward in high-resolution, unstructured-grid sea ice modelling at CMCC. It provides a powerful and adaptable platform for exploring polar and subpolar processes and offers a solid foundation for future developments within next-generation digital ocean twin initiatives.

BIBLIOGRAPHY

[1] C. M. Bitz and W. H. Lipscomb. An energy-conserving thermodynamic model of sea ice. *Journal of Geophysical Research: Oceans*, 104(C7):15669–15677, 1999.

[2] Sylvain Bouillon, Thierry Fichefet, Vincent Legat, and Gurvan Madec. The elastic-viscous-plastic method revisited. *Ocean Modelling*, 71:2–12, 2013.

[3] B.P. Briegleb and B. Light. A Delta-Eddington multiple scattering parameterization for solar radiation in the sea ice component of the Community Climate System Model. Technical report, National Center for Atmospheric Research, NCAR/TN-472+STR, 2006.

[4] F. Cappello, S. Di, R. Underwood, D. Tao, J. Calhoun, Y. Kazutomo, K. Sato, A. Singh, L. Giraud, E. Agullo, X. Yepes, M. Acosta, S. Jin, J. Tian, F. Vivien, B. Zhang, K. Sano, T. Ueno, T. Grützmacher, and H. Anzt. Multifacets of lossy compression for scientific data in the joint-laboratory of extreme scale computing. *Future Generation Computer Systems*, 2024.

[5] CICE Consortium. *Icepack Documentation*. CICE Consortium, 2024. https://app.readthedocs.org/projects/cice-consortium-icepack/downloads/pdf/latest/. Accessed: April 8, 2025.

[6] F. Cocetta, L. Zampieri, J. Selivanova, and D. Iovino. Assessing the representation of Arctic sea ice and the marginal ice zone in ocean–sea ice reanalyses. *The Cryosphere*, 18(10):4687–4702, 2024.

[7] S. Danilov, D. Sidorenko, Q. Wang, and T. Jung. The finite-volume sea ice-ocean model (FESOM2). *Geoscientific Model Development*, 10(2):765–789, 2017.

[8] A. K. DuVivier, M. M. Holland, L. Landrum, H. A. Singh, D. A. Bailey, and E. A. Maroon. Impacts of sea ice mushy thermodynamics in the Antarctic on the coupled earth system. *Geophysical Research Letters*, 48(18):e2021GL094287, 2021.

[9] ECMWF. IFS Documentation CY41R1 - Part iv: Physical Processes. Technical report, ECMWF, 2015. https://www.ecmwf.int/node/9211.

[10] H. Eicken. Salinity profiles of Antarctic sea ice: Field data and model results. *Journal of Geophysical Research: Oceans*, 97(C4):5501–5511, 1992.

[11] Darren Engwirda. JIGSAW-GEO (1.0): locally orthogonal staggered unstructured grid generation for general circulation modelling on the sphere. *Geoscientific Model Development*, 10(6):2117–2140, 2017.

[12] C. W. Fairall, E. F. Bradley, J. E. Hare, A. A. Grachev, and J. B. Edson. Bulk parameterization of air-a fluxes: Updates and verification for the COARE algorithm. *Journal of Climate*, 16(4):571–591, 2003.

[13] Gregory M. Flato and William D. Hibler. Ridging and strength in modeling the thickness distribution of Arctic sea ice. *Journal of Geophysical Research: Oceans*, 100(C9):18611–18626, 1995.

[14] D. Flocco, D. L. Feltham, and A. K. Turner. Incorporation of a physically based melt pond scheme into the sea ice component of a climate model. *Journal of Geophysical Research: Oceans*, 115(C8), 2010.

[15] D. Flocco, D. Schroeder, D. L. Feltham, and E. C. Hunke. Impact of melt ponds on Arctic sea ice simulations from 1990 to 2007. *J. Geophys. Res.*, 117(C9):0148–0227, 2012.

[16] GEBCO Bathymetric Compilation Group. *The GEBCO_2022 Grid – A continuous terrain model of the global oceans and land*. NERC EDS British Oceanographic Data Centre NOC, 2022.

[17] H. Hersbach, B. Bell, P. Berrisford, G. Biavati, A. Horányi, J. Muñoz Sabater, J. Nicolas, C. Peubey, R. Radu, I. Rozum, D. Schepers, A. Simmons, C. Soci, D. Dee, and J-N. Thépaut. ERA5 hourly data on single levels from 1940 to present. Technical report, Copernicus Climate Change Service (C3S) Climate Data Store (CDS), 2023.

[18] W. D. Hibler. A dynamic thermodynamic sea ice model. *Journal of Physical Oceanography*, 9(4):815–846, 1979.

[19] E. Hunke, R. Allard, D. A. Bailey, P. Blain, A. Craig, F. Dupont, A. DuVivier, R. Grumbine, D. Hebert, M. Holland, N. Jeffery, J.-F. Lemieux, R. Osinski, T. Rasmussen, M. Ribergaard, L. Roach, A. Roberts, A. Steketee, M. Turner, and M. Winton. Cice-Consortium/Icepack: Icepack 1.5.0., 2024. doi: 0.5281/ZENODO.1213462.

[20] E. C. Hunke and J. K. Dukowicz. An Elastic-Viscous-Plastic model for sea ice dynamics. *Journal of Physical Oceanography*, 27(9):1849–1867, 1997.

[21] E. C. Hunke, D. A. Hebert, and O. Lecomte. Level-ice melt ponds in the los alamos sea ice model, CICE. *Ocean Modelling*, 71:26–42, 2013.

[22] E. C. Hunke and W. H. Lipscomb. CICE: The Los Alamos Sea Ice Model User's Manual, version 4. Technical Report LA-CC-06-012, Los Alamos National Laboratory, 2008.

[23] B.G. Kauffman and W.G. Large. The CCSM coupler, version 5.0.1. *NCAR Technical Note*, 2002.

[24] M. Kimmritz, S. Danilov, and M. Losch. On the convergence of the modified elastic-viscous-plastic method for solving the sea ice momentum equation. *Journal of Computational Physics*, 296:90–100, 2015.

[25] P. Korn, N. Brüggemann, J. H. Jungclaus, S. J. Lorenz, O. Gutjahr, H. Haak, L. Linardakis, C. Mehlmann, U. Mikolajewicz, D. Notz, D. A. Putrasahan, V. Singh, J.-S. von Storch, X. Zhu, and J. Marotzke. ICON-O: The ocean component of the ICON Earth System Model-Global simulation characteristics and local telescoping capability. *Journal of Advances in Modeling Earth Systems*, 14(10), 2022.

[26] W. G. Large and S. G. Yeager. The global climatology of an interannually varying air-sea flux data set. *Climate Dynamics*, 33:341–364, 2009.

[27] Jean-François Lemieux and Frédéric Dupont. On the calculation of normalized viscous-plastic sea ice stresses. *Geoscientific Model Development*, 13(3):1763–1769, 2020.

[28] William H. Lipscomb, Elizabeth C. Hunke, Wieslaw Maslowski, and Jaromir Jakacki. Ridging, strength, and stability in high-resolution sea ice models. *Journal of Geophysical Research: Oceans*, 112(C3), 2007.

[29] R. Löhner. An adaptive finite element scheme for transient problems in CFD. *Computer Methods in Applied Mechanics and Engineering*, 61(3):323–338, 1987.

[30] G. Micaletto, I. Barletta, S. Mocavero, I. Federico, I. Epicoco, G. Verri, G. Coppini, P. Schiano, G. Aloisio, and N. Pinardi. Parallel implementation of the shyfem (system of hydrodynamic finite element modules) model. *Geoscientific Model Development*, 15(15):6025–6046, 2022.

[31] C. L. Parkinson and N. E. DiGirolamo. Sea ice extents continue to set new records: Arctic, Antarctic, and global results. *Remote Sensing of Environment*, 267:112753, 2021.

[32] M. R. Petersen, X. S. Asay-Davis, A. S. Berres, Q. Chen, N. Feige, M. J. Hoffman, D. W. Jacobsen, P. W. Jones, M. E. Maltrud, S. F. Price, T. D. Ringler, G. J. Streletz, A. K. Turner, L. P. Van Roekel, M. Veneziani, J. D. Wolfe, P. J. Wolfram, and J. L. Woodring. An evaluation of the ocean and sea ice climate of E3SM using MPAS and interannual CORE–II forcing. *Journal of Advances in Modeling Earth Systems*, 11(5):1438–1458, 2019.

[33] J. R. Reagan, T. P. Boyer, H. E. García, R. A. Locarnini, O. K. Baranova, C. Bouchard, S. L. Cross, A. V. Mishonov, C. R. Paver, D. Seidov, Z. Wang, and D. Dukhovskoy. World Ocean Atlas 2023. Technical report, NOAA National Centers for Environmental Information, 2024.

[34] L. A. Roach, C. M. Bitz, C. Horvat, and S. M. Dean. Advances in modeling interactions between sea ice and ocean surface waves. *Journal of Advances in Modeling Earth Systems*, 11(12):4167–4181, 2019.

[35] Lettie A. Roach, Madison M. Smith, and Samuel M. Dean. Quantifying growth of pancake sea ice floes using images from drifting buoys. *Journal of Geophysical Research: Oceans*, 123(4):2851–2866, 2018.

[36] A. Rösel and L. Kaleschke. Exceptional melt pond occurrence in the years 2007 and 2011 on the Arctic sea ice revealed from MODIS satellite data. *Journal of Geophysical Research: Oceans*, 117(C5), 2012.

[37] D. A. Rothrock. The energetics of the plastic deformation of pack ice by ridging. *Journal of Geophysical Research*, 80(33):4514–4519, 1975.

[38] P. Scholz, D. Sidorenko, S. Danilov, Q. Wang, N. Koldunov, D. Sein, and T. Jung. Assessment of the Finite-VolumE Sea ice-Ocean Model (FESOM 2.0) - Part 2: Partial bottom cells, embedded sea ice and vertical mixing library CVMix. *Geoscientific Model Development*, 15(2):335–363, 2022.

[39] P. Scholz, D. Sidorenko, O. Gurses, S. Danilov, N. Koldunov, Q. Wang, D. Sein, M. Smolentseva, N. Rakowsky, and T. Jung. Assessment of the Finite-volumE Sea ice-Ocean Model (FESOM 2.0) - Part 1: Description of selected key model elements and comparison to its predecessor version. *Geoscientific Model Development*, 12(11):4875–4899, 2019.

[40] Albert J. Semtner. A model for the thermodynamic growth of sea ice in numerical investigations of climate. *Journal of Physical Oceanography*, 6(3):379–389, 1976.

[41] A. S. Thorndike, D. A. Rothrock, G. A. Maykut, and R. Colony. The thickness distribution of sea ice. *Journal of Geophysical Research*, 80(33):4501–4513, 1975.

[42] A. K. Turner, E. C. Hunke, and C. M. Bitz. Two modes of sea-ice gravity drainage: A parameterization for large-scale modeling. *Journal of Geophysical Research: Oceans*, 118(5):2279–2294, 2013.

[43] M. Vancoppenolle, C. Rousset, E. Blockley, Y. Aksenov, D. Feltham, T. Fichefet, G. Garric, V. Guémas, D. Iovino, S. Keeley, G. Madec, F. Massonnet, Jeff Ridley, D. Schroeder, and S. Tietsche. SI3, the NEMO sea ice engine. 2023. https://zenodo.org/record/7534900.

[44] X. Yepes-Arbós, G. van den Oord, M. C. Acosta, and G. D. Carver. Evaluation and optimisation of the I/O scalability for the next generation of earth system models: IFS CY43R3 and XIOS 2.0 integration as a case study. *Geoscientific Model Development*, 15(2):379–394, 2022.

[45] L. Zampieri, F. Kauker, Jörg Fröhle, H. Sumata, E. C. Hunke, and H. F. Goessling. Impact of sea-ice model complexity on the performance of an unstructured-mesh sea-ice/ocean model under different atmospheric forcings. *Journal of Advances in Modeling Earth Systems*, 13(5), 2021.

[46] X. Zeng and A. Beljaars. A prognostic scheme of sea surface skin temperature for modeling and data assimilation. *Geophysical Research Letters*, 32(14):1944–8007, 2005.

[47] J. Zhang, A. Schweiger, M. Webster, B. Light, M. Steele, C. Ashjian, R. Campbell, and Y. Spitz. Melt pond conditions on declining Arctic sea ice over 1979-2016: Model development, validation, and results. *Journal of Geophysical Research: Oceans*, 123(11):7983–8003, 2018.
